

Article

# A Compact Adjustable Stiffness Rotary Actuator Based on Linear Springs: Working Principle, Design, and Experimental Verification

Cong Phat Vo , Van Du Phan , Thanh Ha Nguyen  and Kyoung Kwan Ahn \*

School of Mechanical and Automotive Engineering, University of Ulsan, Ulsan 44610, Korea;  
vophat0607@gmail.com (C.P.V.); dupv@vinhuni.edu.vn (V.D.P.); nthanhha12c4@gmail.com (T.H.N.)

\* Correspondence: kkahn@ulsan.ac.kr; Tel.: +82-52-259-2282

Received: 14 November 2020; Accepted: 14 December 2020; Published: 18 December 2020



**Abstract:** Inspired by improving the adaptive capability of the robot to external impacts or shocks, the adjustable stiffness behavior in joints is investigated to ensure conformity with the safety index. This paper proposes a new soft actuation unit, namely Adjustable Stiffness Rotary Actuator (ASRA), induced by a novel optimization of the elastic energy in an adjusting stiffness mechanism. Specifically, a stiffness transmission is configured by three pairs of antagonistically linear springs with linkage bars. The rotational disk and link bars assist the simplified stiffness control based on a linear transmission. To enhance the elastic energy efficiency, the force compressions of the linear springs are set to be perpendicular to the three-spoke output element, i.e., the output link direction. Besides, the ASRA model is also formed to investigate the theoretical capabilities of the stiffness output and passive energy. As a simulated result, a high passive energy storage ability can be achieved. Then, several experimental scenarios are performed with integral sliding mode controllers to verify the physical characteristics of the ASRA. As trial results, the fast transient response and high accuracy of both the position and stiffness tracking tests are expressed, in turn, independent and simultaneous control cases. Moreover, the real output torque is measured to investigate its reflecting stiffness.

**Keywords:** Adjustable Stiffness Rotary Actuator; variable stiffness transmission mechanism; energy efficiency

---

## 1. Introduction

Traditional robotics mostly use stiff actuators to perform movement tasks. However, such an actuator does not guarantee the safety requirement as well as the quality performance in the cases of human contact or complicated environments. In order to deal with the drawback, a variable stiffness strategy based on a mechanical mechanism has been introduced in many studies [1–7], which has high feasibility for compliant robots [8,9]. To be more specific, the stiffness feature of the joint can be altered by an adjustment agent such as springs, which is not only guaranteed safety to humans and avoided destruction to the robot [10–15], but also the simultaneously controllable ability of both the position and stiffness [16,17]. Much research effort has been made on the development of these variable stiffness actuators (VSA). Therefore, many different mechanisms have been designed for different applications. Thus, to get an overview, the VSA design principles have been broadly considered. From this perspective, the elastic elements of current VSA designs can be temporarily divided into two arrangement forms as serial configuration and antagonistic configuration [18,19].

A well-known example of the serial-configured VSA is a series elastic actuator (SEA) in which the mechanical compliance elements were serially linked to the controllable equilibrium position actuators [20–24]. In order to conduct a straightforward process for this purpose, at least two

different actuators are separately required. In detail, one actuator takes over the position control and another one adjusts the stiffness, which is assisted by elastic elements [24–27]. The outstanding features of this mechanism design are the high actual bandwidth and great faithfulness of the output torque. Those characteristics are relatively suitable to be embedded in compliant robots [11, 28]. Nevertheless, the energy efficiency of such series-configured VSA degraded when adjusting the stiffness transmission [29]. A variable stiffness joint (VSJ) was introduced in Reference [30], where four-leaf springs are fixed in the principal axis and set perpendicularly to each other. Based on the harmonic gear mechanism, the distance between the rollers and the principal axis is adjusted. It means that the effective length of the spring, as well as the joint stiffness, is modified. In Reference [31], another structure was designed to change effective stiffness using the torsion spring (TSA). The stiffness adjustment was mounted to the wire-rope and idle pulleys, which were driven by the cam-bearing followers. Here, the torsion springs make a sliding groove for the cam-bearing followers, which assisted the rollers. Nonetheless, the general drawback of the aforementioned prototypes (VSJ, TSA, AwAs [6], etc.) was the limited range of the stiffness adjustment in a specific region of activity, owing to the intrinsic elastic unit. What is more, the torsion springs are used in most variable stiffness rotary actuators, where the variable stiffness mechanism could affect the position of the output link. In the meantime, several designs employed the linear spring, leading to a more complicated structure. For the antagonistic-configuration VSA perspectives, the compliant component consists of one or more pairs of elastic elements [32–35], which were mounted together in imitating the skeletal muscle of human joints to drive position as well as modify stiffness output. Nonetheless, the shortcoming of this designed structure could affect not only the control synchronization but also the position of the output link.

In order to overcome the above drawback, this paper designs a novel compact Adjustable Stiffness Rotary Actuator (ASRA) according to a new adjusting stiffness mechanism, which is controlled independently of the position control system. Moreover, the total system structure is not only a simple design, but also high-energy storage based on intelligent mechanical design, which is a potential generic solution of the compliance module. Specifically, the variable stiffness transmission employs three pairs of linear springs with an antagonistic arrangement to realize the stiffness adjustment. Besides, it should be emphasized that the configuration of the externally affected force direction is perpendicular to the spring force compression. Hence, the proposed actuator exhibits significant improvements over the present designs based on torsion spring or extension springs/cable assemblies. Additionally, the mathematical model of the ASRA is also formed to verify a high passive energy storage ability in simulation. Then, a series of experimental scenarios for both the position and stiffness tracking task, including independent and simultaneous control, is established to investigate the physical characteristics of the ASRA.

The structure of this paper is as follows. Section 2 presents the working principle, mechanical design, and prototype fabrication of the proposed actuator. Section 3 describes the modeling and simulation of the ASRA. Then, the operation principle and the control scheme are exhibited in Section 4. The experimental results of the ASRA are carried out to evaluate in Section 5. Finally, the conclusions and future works are provided in Section 6.

## 2. Mechanical Design of the ASRA

In this section, a new design of the ASRA based on antagonistic pairs of the compression springs is presented. The three circular modules are evenly arranged on a circle and moved on a radial trajectory at the same time as the motor spins. Six linear springs are always compressed or released at the same time and with the same amount by the new stiffness transmission mechanism design, which modifies independently with the position control system.

### 2.1. Design Description

The detail of the adjusting stiffness mechanism is depicted in Figure 1a. The lead screw (4) is fixed to the shaft of the motor (2) using the coupling (3). The upper side of the rotary disk (7) is coupled

to the screw nut (5) by the long bar (6). Meanwhile, the lower side is engaged with three circular modules (12) by three short bars (9). These circular modules are mounted on the six linear springs (10), which can slide on the three guiding bars (14). The six linear springs are divided into three antagonistic pairs, which are coupled with the three-stroke output element (11). The three-spoke output element is toughly connected to the output link (1). Figure 1b shows the design of the proposed ASRA in a one-degree-of-freedom (1-DOF) system. As shown in this figure, the main components of the system consist of a base (16) as the first link, a cylinder (15) as the positioning actuator, a motor as the adjusting stiffness actuator, a set of bearings (8), and an adjusting stiffness mechanism inside the intermediate link (13).

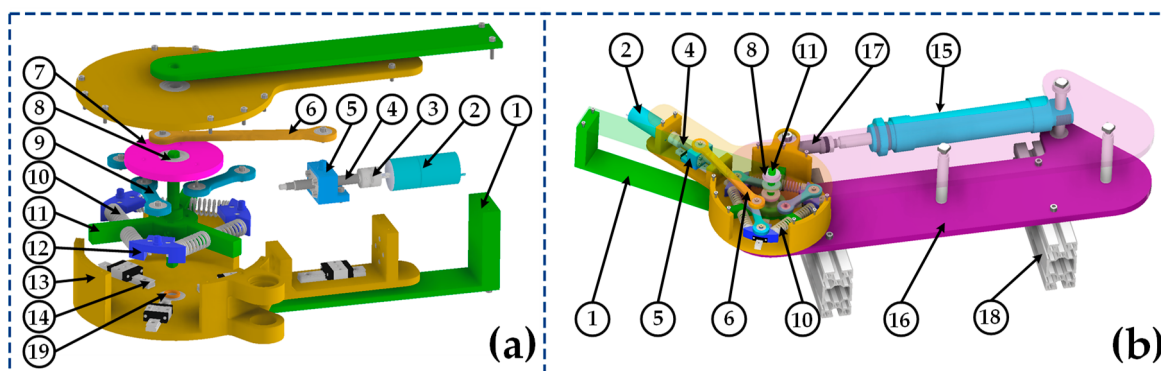


**Figure 1.** Three-dimensional (3D) model of the one-degree-of-freedom (1-DOF) manipulator with the Adjustable Stiffness Rotary Actuator (ASRA): (a) Explosive view. (b) Full sectional view. 1—Output Link, 2—Adjusting stiffness motor, 3—Coupling, 4—Lead screw, 5—Screw nut, 6—Long bar, 7—Rotary disk, 8—Bearing, 9—Short bar, 10—Linear spring, 11—Three-spoke output element, 12—Circular module, 13—Intermediate link, 14—Guiding bar, 15—Principal cylinder, 16—Base, 17—Shaft coupling, 18—Aluminum sole, 19—Thrust bearing.

In order to provide an effective torque for the output link, each spoke of the three-spoke output element is coupled perpendicularly with each pair of linear springs. Thus, the output link direction suffers from the optimal compression force of the total springs. It should be noted that the operation of the adjustable stiffness mechanism does not affect the position of the joint thanks to the ability of compliant actuator design. Additionally, this mechanism is designed without the gear transmission, the internal friction has been significantly alleviated during the operation process of the inside rotational elements with the assistance of ball bearings, which plays an important role in increasing the elastic energy storage. Moreover, this proposed actuator is completely feasible in the case of the robot–environment interaction with a fast collision or high force peaks. Besides, the compact ASRA is capable to deal with the collision and also absorb the effect of the impact. In particular, the adjusting stiffness at constant load is crucial since the slight force interaction with the environment is desired. On the other hand, the adjusting stiffness at a constant position helps the robot system maintain a low position error in the presence of disturbances by a proportional valve.

It is worth noting that the range of the angle deflection is not influenced by the mechanical transmission including a disk or link bars. Therefore, this angle deflection can be measured by the deviation between the principal cylinder and the actual output position of the ASRA, which is limited to  $28.6^\circ$  in the minimum stiffness condition. The component specifications of the ASRA are listed in detail in Table 1 Furthermore, the stiffness ranges from zero to infinity, so that theoretically, the deflection angle is nonexistent.

**Table 1.** General specifications of the ASRA.

Parameter	Description	Value	Unit
$\theta$	Angular deflection between an immediate link and output link	28.6	degree
$r$	Radius of the rotary disk	25	mm
$d_0$	Initial length in case of maximum cylinder retracting	230	mm
$y$	Motion range of the cylinder	80	mm
$d_1$	Length of the long hinge joint	100	mm
$d_2$	Length of the short hinge joint	300	mm
$l$	Range of motion of the circular module	10	mm
$L$	Initial length of the spring	40	mm
$L_1$	Compression length of each pair of the springs		
$L_2$	Extension length of each pair of the springs		
$R$	Distance from an applied force of springs to the joint center	40	mm
$\eta$	Ratio lead of the lead screw	2	mm
$n$	Ratio of the gearbox	35:1	
$a$	Initial distance from the circular module to a rotary joint center	56.5	mm
	Weight of the ASRA	0.677	kg
$b$	Long bar length	130	mm
$d$	Short-bars length	52	mm
$c$	Range of motion of the screw nut	25	mm
$K_s$	Inherent spring stiffness	4650	N/m

## 2.2. Working Principle

The working principle of the proposed adjustable stiffness mechanism is depicted in Figure 2. The lead screw shaft is rotated with the spin of the motor shaft through the coupling. The rotational motion of the screw shaft is translated to the linear motion of the screw nut, which then pushes or pulls the long bar to move. The motion of the long bar leads to the rotational motion of the disk. Then, the motion of the rotary disk is converted to the linear motion of three circular modules along the rails, which simultaneously compresses or releases the set of six linear springs.

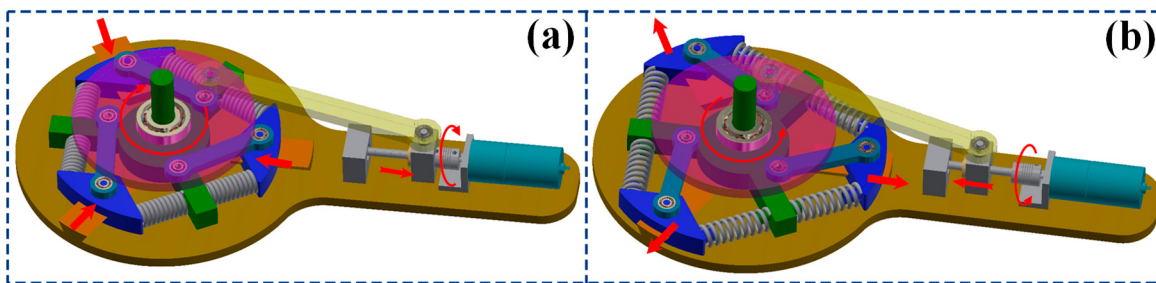


**Figure 2.** Principle of the ARSA based on the motion of the rotary disk to linear motion of three circular modules along the rails. (a) Decreased stiffness. (b) Increased stiffness.

As seen in Figure 2a, the motor spins with a clockwise motion and turns the lead screw by the coupling, which makes the screw nut move toward the motor. Hence, the rotary disk is forced to rotate in a clockwise direction. Successively, the three circular modules are pulled into the center of the disk through the three short bars and guiding bars, which compress six linear springs concurrently. Thus, the connection between the intermediate link and the output link becomes “stiff”. In other words, if the springs are compressed enough, the intermediate link and the output link could be fixed together, and the actuator becomes a conventional “stiff” one. In contrast, the motor shaft spins in a counterclockwise direction, which makes the screw nut move away from the motor and forces the rotary disk to rotate in the opposite direction. The three circular modules are then pushed to simultaneously move away from the center of the disk and release the six springs. The three-spoke output element can now oscillate with respect to the intermediate link, thus making the actuator become “soft”, as shown in Figure 2b. In this mechanism design, the three circular modules are evenly

arranged on a circle and move on a radial trajectory at the same time as the motor spins. It implies that the six springs are always compressed or released with the same amount in synchronization. Therefore, this design of a stiffness adjustment mechanism can be operated independently with the position control system.

### 2.3. Prototype Fabrication

In order to endorse the perspective on the effectiveness of the ASRA, a prototype is fabricated in Figure 3. In detail, the pairs of the spring are separated for each spoke module to enhance the energy storability: they are selected with an initial length  $L$  and an inherent stiffness  $K_s$ . It may be noted that the general size of the actuator needs to be optimal. Thus, the suitable distance  $R$  from the applied spring forces on the three-spoke output element to the joint center is considered in the design requirement. Additionally, the three-spoke element shape, the radius  $r$  of the rotary disk, the link bar lengths, i.e., the connection point with the long  $b$  and short bars  $d$ , are authentically calculated to provide a sync motion.

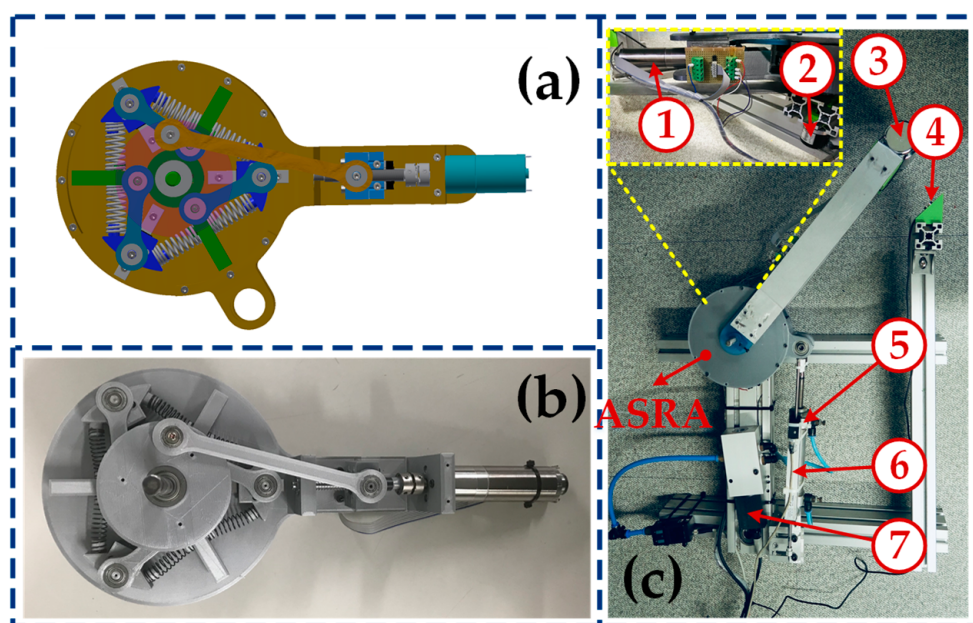


**Figure 3.** The test rig fabrication of the flexible joint induced by ASRA: (a) The ASRA design; (b) The ASRA reality; (c) the flexible joint induced by ASRA. 1—Motor, 2—Optical encoder, 3—Load, 4—Loadcell, 5—Cylinder, 6—Position transducer, 7—Proportional valve.

Therefore, the specification of the experimental devices is listed in Table 2. A brushless direct current motor (model: Maxon DCX26L-GB-KL-24V, 60 W, Stock Company, Obwalden, Switzerland) with a gearbox ratio of 35:1 is adopted as a stiffness control motor. A capacitive encoder is integrated on the rear of the motors with 4096 pulses per revolution to measure the position of the motor, which manages the theoretical stiffness. An optical encoder (model: E40H12-1024-3-V-5, Autonics, Korea) with a revolution of 1024 pulses per turn is mounted to determine the actual output link position. Meanwhile, the position of the principal cylinder can be determined by the position transducer (model: TR-100, Novotechnik, Ostfildern, Germany). The control pressure of the cylinder is achieved by a proportional valve (MPYE-5-1/8-LF-010-B, Festo Company, Seoul, Korea). In addition, the joint interacting torque is measured by a torque sensor (Bongshin CDFSA). The control system setup is deployed as a standalone device using a PC programmable through NI-6229 card and QUAD-04 card. The system is built in a real-time Windows target toolbox on the MATLAB-Simulink environment and a sampling time of 0.005 s.

**Table 2.** Specifications of the experimental devices.

Device	Description
Motor	Type: Maxon DCX26L-GB-KL-24V with Gear ratio: 35:1 Nominal speed: 5060 rpm; Nominal torque: 32.6 mNm Optical encoder: 4096 pulses/rev
Cylinder	Type: Festo DSNU-S-16-25-P-A Piston diameter: 20 mm; Stroke length: 100 mm
Motor driver	Type: Robot Electronics MD-03 Power supply: 24 V, 20 A
PPR Valve	Type: Festo MPYE-5-1/8-LF-010-B Max pressure: 10 bar; Power supply: 24 V
DAQ Card	NI-6229 AI/AO: 12 bits (resolution) MEASUREMENT PCI-QUAD04
Loadcell	Type: Bongshin CDFSA-10; Rated output: 1.0 mV/V
Position transducer	Type: TR-100; Length: 100 mm
Rotary encoder	Type: E40H12-1024-3-V-5; Resolution: 4096 pulses

### 3. Design ARSA for the Flexible Joint

#### 3.1. Dynamic Model

This subsection described the dynamic model of the flexible joint induced by ASRA. Based on the schematic illustrated in Figure 4, the movement equation can be formed as follows:

$$\begin{cases} M_0\ddot{q} + B_0\dot{q} + \tau_o = \tau_e \\ M_1\ddot{q}_1 + B_1\dot{q}_1 - \tau_o = \tau_p \\ M_2\ddot{q}_2 + B_2\dot{q}_2 + \tau_k = \tau_m \end{cases} \quad (1)$$

where  $M_i, B_i$  ( $i = 0, 1, 2$ ) denotes the total inertias and damping respectively (the output link, the position and stiffness control actuators with gearbox, and other mechanisms),  $q, q_1$ , and  $q_2$  are the positions, in turn, of the output link, the cylinder, and the adjustable stiffness motor,  $\tau_p$  and  $\tau_m$  are the torque required by the cylinder and the stiffness motor respectively,  $\tau_e$  is the external torque on the output link, and  $\tau_o$  and  $\tau_k$  are the torques of the elastic spring and resistance, respectively.

As shown in Figure 4c, the correlation between the motion of the cylinder  $y$  and the joint angle of output link  $q$  can be derived by:

$$y = \sqrt{d_1^2 + d_2^2 - 2d_1d_2\cos(\pi - q_1)} - d_0 \quad (2)$$

where  $d_0$  and  $y$  denote the initial length in a maximum retracting and the end-effector position under the cylinder act, and  $d_1$  and  $d_2$  are the fixed length of the hinge links.

To acquire the relation velocity between the actuator and the joint motion, take the derivative of (2) with respect to time, as follows:

$$\dot{y} = \frac{\partial y}{\partial q_1}\dot{q}_1 = \frac{d_1d_2\sin(\pi - q_1)}{\sqrt{d_1^2 + d_2^2 - 2d_1d_2\cos(\pi - q_1)}}\dot{q}_1 = J(q_1)\dot{q}_1 \quad (3)$$

where  $J(q_1)$  is a Jacobian value of the joint.

Therefore, a principal torque acting on the joint can be formed as:

$$\tau_p = J^T(q_1)(F_p - F_f) \quad (4)$$

where  $F_P = P_1A_1 - P_2A_2$  is the force on the piston including the air pressure,  $P_j$ , and the piston area,  $A_j$ , ( $j = 1, 2$ ) in the  $j^{th}$  chamber, and  $F_f$  derives the friction of the piston rod. Based on Reference [36], the relationship between the cylinder force and an input signal is provided as follows:

$$F_P = K_c u \quad (5)$$

where  $K_c$  is a control coefficient and  $u$  is the control input signal.

Additionally, the maximum value of the joint angle is constrained by the length of the cylinder  $y_{max}$  in the case of maximum extending. Thus, the motion range of the flexible joint can be defined as:

$$\cos^{-1}\left(\frac{d_1^2 + d_2^2 - d_0}{2d_1d_2}\right) \leq \pi - q_1 \leq \cos^{-1}\left(\frac{d_1^2 + d_2^2 - (d_0 + y_{max})}{2d_1d_2}\right) \quad (6)$$

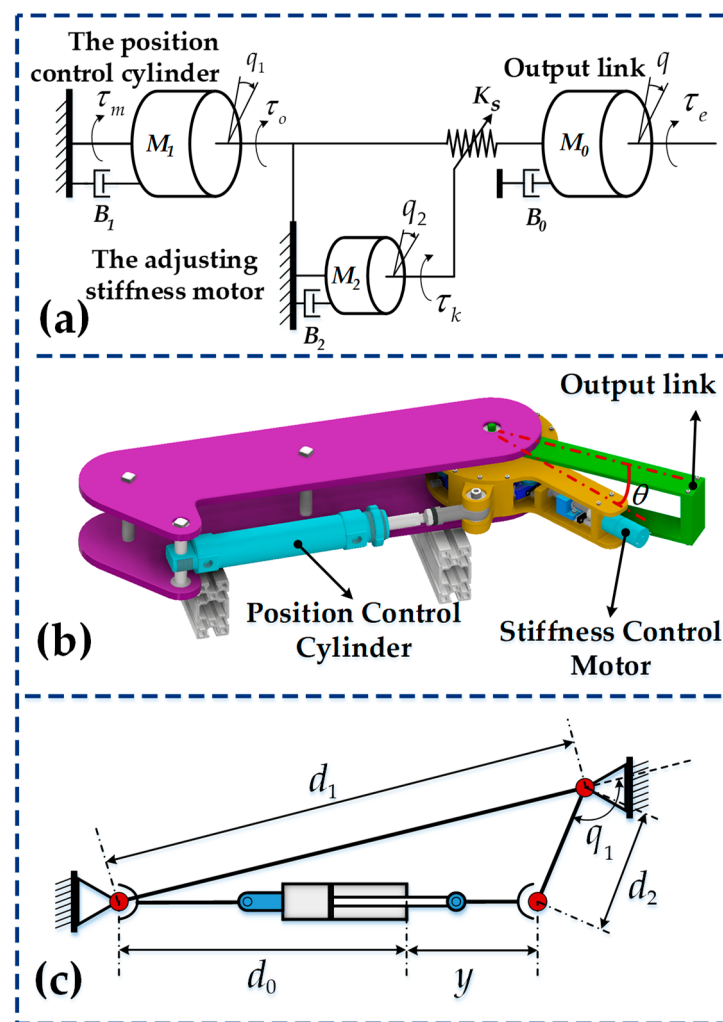


**Figure 4.** The flexible joint is induced by the ASRA schematic: (a) Structural model; (b) Three-dimensional design; (c) The architecture of the joint.

### 3.2. Stiffness Model

This subsection defines the adjustment stiffness model of the ASRA. To start with, the output link is fixed to the three-spoke module, when any external impacts occur to the spoke spring structure, the springs will be compressed or extended as shown in Figure 5. Considering a pair of the antagonist linear springs (see in Figure 5a), the axial forces are generated by each of the springs when the complaint

three-spoke module (see in Figure 5b) is diverted from the equilibrium position by a deflection angle of  $\theta$  (see in Figure 5c). These forces can be defined as follows.

$$\begin{cases} F_1 = K_s(L - L_1) \\ F_2 = K_s(L - L_2) \end{cases} \quad (7)$$

where  $L_1 = \sqrt{a^2 + R^2 - 2aR\cos(60^\circ - \theta)}$ ,  $L_2 = \sqrt{a^2 + R^2 - 2aR\cos(60^\circ + \theta)}$  and  $a = \sqrt{L^2 + R^2} - l$ .

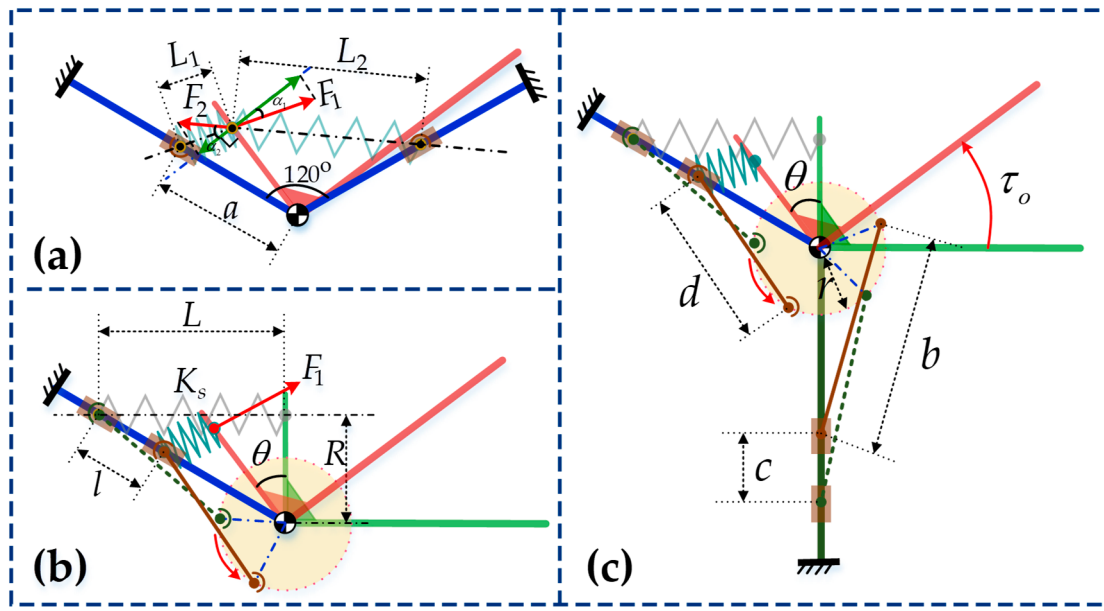


**Figure 5.** Schematic diagram of the stiffness adjustment principle: (a) A pair of forces applied on the three-spoke output element; (b) Effect of the rotary disk; (c) Stiffness will change when the screw nut slides up and down;  $a$  is the initial distance from the circular module to the joint center,  $R$  is the distance from the applied force of springs to the joint center,  $L$  is the initial length of the spring,  $l$  is the motion range of the circular module,  $L_1$  and  $L_2$  are the compression and extension length of each pair of the springs respectively,  $\theta$  is deflection angle between the output link and the immediate link,  $\alpha_1$  and  $\alpha_2$  are the deflection angles of the applied force spring in the three-spoke element respectively,  $r$  is the radius of the rotary disk,  $b$  and  $d$  are the lengths of the long and short bars respectively, and  $c$  is the motion range of the screw nut.

Successively, the axial force applied in each spoke is gathered as follows:

$$F = F_1 \cos \alpha_1 - F_2 \cos \alpha_2 \quad (8)$$

where  $\alpha_1 = \cos^{-1}\left(\frac{L^2 + R^2 - a^2}{2L_1 R}\right) - 90^\circ$  and  $\alpha_2 = 90^\circ - \cos^{-1}\left(\frac{L^2 + R^2 - a^2}{2L_2 R}\right)$ .

Then, the elastic energy storage at the compression springs is formed as follows:

$$E = 3 \int_0^x F dx = 3K_s(x_1^2 + x_2^2) = 3K_s \left[ \left( L - \sqrt{R^2 - 2\gamma_1 Ra + a^2} \right)^2 + \left( L - \sqrt{R^2 - 2\gamma_2 Ra + a^2} \right)^2 \right] \quad (9)$$

where  $x_i = L - L_i$ , ( $i = 1, 2$ ),  $\gamma_1 = \cos(\theta - \pi/3)$  and  $\gamma_2 = \cos(\theta + \pi/3)$ .

Thus, the elastic torque can be formulated as:

$$\tau_o = \frac{\partial E}{\partial \theta} = -3K_s \left[ \frac{2\gamma_3 Ra \left( L - \sqrt{R^2 - 2\gamma_1 Ra + a^2} \right)}{\sqrt{R^2 - 2\gamma_1 Ra + a^2}} + \frac{2\gamma_4 Ra \left( L - \sqrt{R^2 - 2\gamma_2 Ra + a^2} \right)}{\sqrt{R^2 - 2\gamma_2 Ra + a^2}} \right] \quad (10)$$

where  $\gamma_3 = \sin(\theta - \pi/3)$  and  $\gamma_4 = \sin(\theta + \pi/3)$ .

Besides, the joint stiffness is obtained by taking the derivative of (10) with respect to the angular deflection of  $\theta$ , which can be described as:

$$K_j = \frac{\partial \tau_o}{\partial \theta} = f(q_2, \theta) \quad (11)$$

After defining the properties of the ASRA from (7) to (11), it is noteworthy that its performance is only influenced by two factors, including the position of the circular module and the angular deflection  $\theta$ . Meanwhile, the other parameters are fixed, such as the inherent spring stiffness  $K_s$ , the length of the bars  $b$  and  $d$ , and also the distance from the applied force point of springs to the rotary joint center  $R$ . When the output link is impacted, the ASRA is resisted by the controlled spring length, namely the circular module movement. Therefore, the external torque output is related to the position of the circular module.

The real output position of the flexible joint  $q$  can be straightly determined by an optical encoder through the output link. Consequently, the deflection angle can be extracted from the output position disparity between the cylinder  $q_1$  and the real output link  $q$ .

$$\theta = q - q_1 \quad (12)$$

For this design, the long and short bars are mounted to the rotary disk at the same radius. Thus, the position of the circular modules can be calculated based on the motion range of the screw nut on the lead screw, which is expressed as follows:

$$l = \frac{d \cdot c}{b} = \frac{d \cdot q_2 \cdot \eta \cdot n}{b} \quad (13)$$

where  $q_2$  is the position of the adjusting stiffness motor,  $n$  is the ratio of the gearbox, and  $\eta$  is the ratio of the lead screw. Additionally, the value  $l$  is the range of motion of the circular modules, which is designed. Thus, the range of  $q_2$  should be set as:

$$0 \leq q_2 \leq \frac{l \cdot b}{d \cdot \eta \cdot n} \quad (14)$$

From (7), (8), and (13), the resistance torque for the motor to adjust the stiffness can be calculated as:

$$\tau_k = \frac{b}{d \cdot \eta \cdot n} (F_1 \sin \alpha_1 - F_2 \sin \alpha_2) \quad (15)$$

Figure 6a depicts the simulation results in the output stiffness with the various positions of the circular module. It is easily seen that the larger inherent stiffness has a more effective working range of the ASRA. The intrinsic spring stiffness will thus affect the nonlinearity of the stiffness curve. According to the installation space and the desired stiffness of the output link, the linear spring stiffness is selected at 4.65 kN/m for the proposed prototype. Figure 6b–d express, in turn, the simulation results of the stored elastic energy, the elastic torque, and variable stiffness from the circular module as the range of motion from 2 to 10 mm.

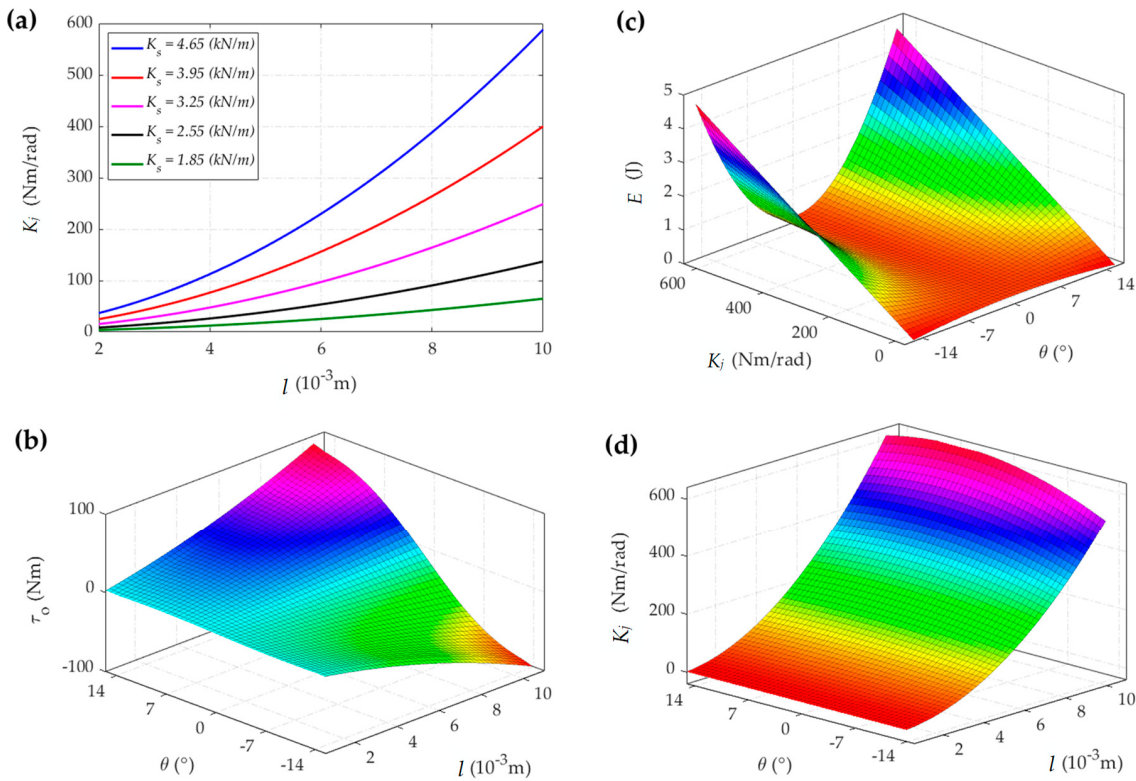


**Figure 6.** The simulation results: (a) The output link stiffness in the variation of intrinsic spring stiffness, (b) elastic torque, (c) elastic energy stored in the spring, and (d) stiffness of the ASRA.

#### 4. Control of the ARSA

In this section, we address the total design procedure of the proposed tracking control for the flexible joint induced by ASRA. In the control procedure, a nonlinear sliding manifold and its attractor dynamics are derived, and tracking control is presented accordingly. The control objective is to generate the input signal for the actuator to behold how its actual position tracks the desired position. The structure of the proposed control is presented in Figure 7. As explained in the above-mentioned analysis, the output stiffness of the actuator is determined by the position  $l$  of the circular module, i.e., inversely solving the stiffness model in (11). In addition, the reference signal block provides the desired trajectory position  $q_{1d}$  and stiffness  $K_d$ . The position controller is responsible for guaranteeing that the principal cylinder follows the desired position trajectory. In the meantime, the stiffness controller handles the errors from the feedback position of the adjustable stiffness motor  $q_2$  and the desired position of the motor  $q_{2d}$ ; before that, the desired position  $q_{2d}$  can be computed by the actual deflection angle  $\theta$  and the desired stiffness  $K_d$ , and this computation is shown in (11). Inspired by the finite-time stability from References [37–39], an integral sliding mode controller (ISMC) is employed. The surface of the ISMC is defined as follows:

$$\sigma_i = e_i + \lambda_{i1} \int_0^t e_i(\chi) d\chi \quad (16)$$

where  $e_i = q_{id} - q_i$  are the position errors between the desired trajectory and the actual response,  $\lambda_{i1}$  is positive coefficients of the sliding surface, and  $i = 1, 2$  implies the signals of the position and stiffness, respectively. After  $q_{1d}$  and  $q_{2d}$  are determined, the control signal will be chosen to perform the experiment trials, as follows:

$$u_{qi} = K_{ic}^{-1} [q_{id} + \lambda_{i1}^{-1} \dot{e}_i + \rho_{i1} \sigma_i + \rho_{i2} \text{sign}(\sigma_i)] \quad (17)$$

where  $\rho_{i1}$  and  $\rho_{i2}$  are positively designed parameters.

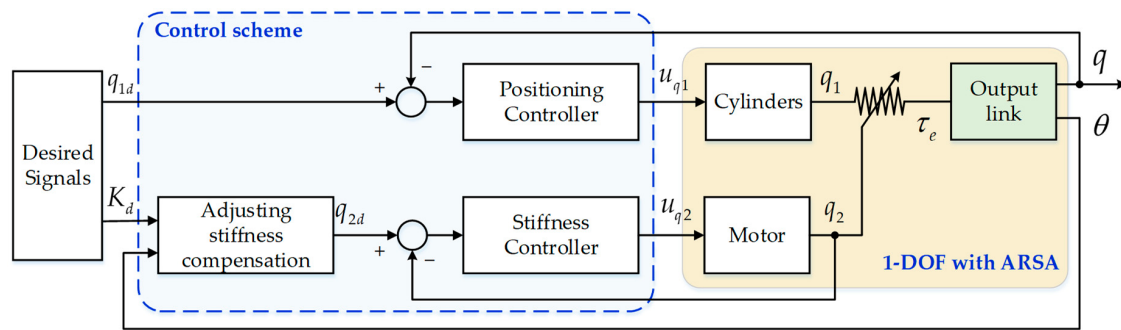


**Figure 7.** Structure of the control scheme for the flexible joint induced by ASRA.

## 5. Experiment and Results

The dynamic model has been commented on in the simulation results by the mathematical equations. Successively, to confirm the characteristics of the ASRA, the one-degree-of-freedom joint test rig is built with the device specifications, which are listed in Table 2. Then, the implementation aspects, including the smooth multi-steps response and the sinusoidal tracking, are carried out to test the position and stiffness variations. It is worth noting that the computed output stiffness in (11) assists to determine the actual output stiffness based on the feedback of the angular deflection  $\theta$  due to the fact that it cannot be directly measured in the actuator. Therefore, the stiffness tracking performance can be evaluated from the position control performance of the stiffness motor through the theoretical stiffness model. In detail, the integral sliding mode controller (ISMC) is applied for the position tracking control. Next, the response performances of the ASRA are analyzed under the no-load condition and the 2 kg load, in which the load is attached to the output link cover for the tracking experiments. Hence, the designed controllers are adopted in this research to control the principal torque based on the cylinder and the motor by adjusting the spring contraction to the desired stiffness. These parameters of the ISMC designed for the system at each actuator are chosen for the position controller  $K_{1c} = 4.5$ ,  $\lambda_{11} = 5$ ,  $\rho_{11} = 2$ ,  $\rho_{12} = 1.5$ , while for the stiffness controller  $K_{2c} = 1.5$ ,  $\lambda_{21} = 6$ ,  $\rho_{21} = 1.25$ ,  $\rho_{22} = 3$ . In order to validate the genuine perspective on the tracking performance of the ASRA in the system, the trial scenarios are separated into the smooth multi-step tracking and the sinusoidal tracking under external load variation. The experimental testbench is established as seen in Figure 3c. Moreover, to verify the reflection of the stiffness, the real output torque measurements are performed.

### 5.1. Smooth Multi-Step Tracking

In the smooth multi-step tracking, the position variation is executed for different loads (no-load and 2 kg load) at the 100 Nm/rad stiffness condition. The desired tracking within the range of  $[0, 40^\circ]$  in different step-time conditions is 10 s. In Figure 8a, the integral absolute errors ( $L_2[e] = \sqrt{\left(\int_0^T |e|^2\right)/T}$ ) where T is the total experimental time, they are approximately  $0.4212^\circ$  and  $0.7768^\circ$  for no-load and 2 kg load, respectively. Therefore, it is easily seen that the time to steady-state and the error amplitudes will be larger when the load is attached. Nevertheless, this drawback can be handled by the suitable controller gains; here, those control parameters are fixed in the experiment. Successively, in Figure 8b, the desired theoretical stiffness with an amplitude variation from 30 Nm/rad to 150 Nm/rad is also examined under the two above-mentioned load conditions. The integral absolute errors for the 2 kg load condition is approximately 0.9866 Nm/rad, which is slightly larger than that for the no-load of 0.8619 Nm/rad. Specifically, more load will enlarge the overshoot amplitude of the system. This result propounds that stiffness control is affected by the external load.

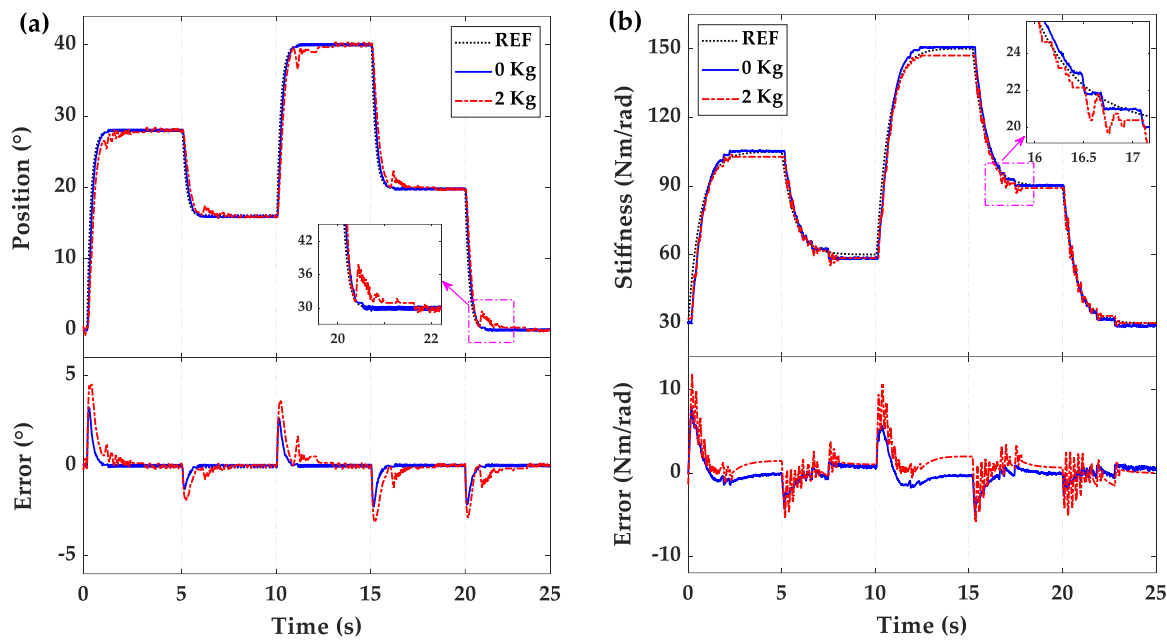


**Figure 8.** Smooth multi-step tracking results: (a) Position control, (b) stiffness control.

### 5.2. Sinusoidal Tracking

In this part, the sinusoidal tracking experiments are divided into three aspects to appraise the tracking performance of the ASRA in the system: independent tracking position and theoretical stiffness, then both for simultaneous tracking, which is exhibited in Figures 9 and 10, respectively. In the first aspect, the position tracking performance is investigated with respect to a sinusoidal amplitude of  $\pm 40^\circ$  at 0.5 Hz under no-load, and an external load of 2 kg is added. Meanwhile, the theoretical stiffness is set to a fixed value of 50 Nm/rad. As a result, Figure 9a exposes that the tracking trajectory has higher accuracy without any load. The bound of the tracking error without load nearly equals two times that of adding the external 2 kg load, from  $\pm 1.85^\circ$  to  $\pm 3.6^\circ$ . These results indicate that the external load gently affects the position tracking performance. Figure 9b depicts the experimental stiffness tracking results at the sinusoidal reference signal with an amplitude from 10 to 130 Nm/rad and a frequency of 0.5 Hz for different loads. The bound of the stiffness tracking error is about 4 Nm/rad, and the integral absolute error is 0.814 Nm/rad without the external load. Meanwhile, the stiffness tracking error amplitude and its integral absolute error expand to 7.5 Nm/rad and 0.9701 Nm/rad, respectively. So, the stiffness tracking response is slightly affected by the external load.

To investigate the ASRA for potential practical applications, the simultaneous tracking is considered for the system under the aforementioned different external load conditions. Hereby, the sinusoidal trajectories of the position and the stiffness are a peak-to-peak of  $\pm 40^\circ$  and a range of 10–130 Nm/rad at the same frequency of 0.4 Hz, respectively. Then, the experimental results are expressed in Figure 10. When the system worked in the no-load condition, the errors of the position tracking and stiffness tracking had peak values of  $4^\circ$  with the integral absolute error of  $0.9785^\circ$  and 5 Nm/rad with the integral absolute error of 1.188 Nm/rad, respectively. After adding the external 2 kg load, the maximum tracking errors increased, in turn, to  $7^\circ$  and 10 Nm/rad, and the associated integral absolute errors expanded to 1.042° and 1.381 Nm/rad. Based on these experimental results, the tracking correctness of both controls for the position and stiffness are slashed by the external load. On the whole, a significant reciprocal intervention can be noticed of the position and stiffness control when compared to quantitative results between the independent and simultaneous performance in the same load condition. This intervention significantly influences not only the effectiveness of the tracking control but also an opportunity in terms of simultaneous controller development.

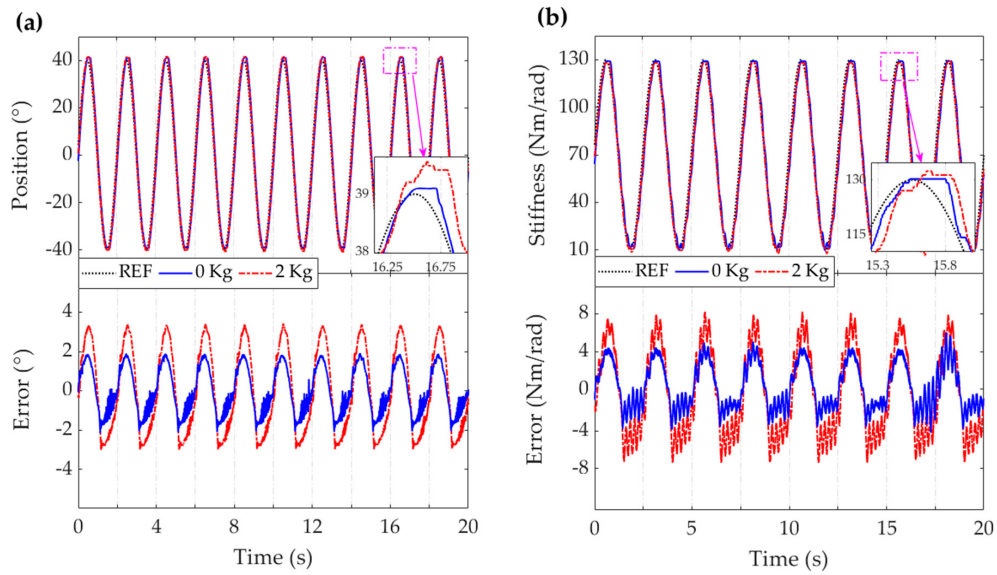


**Figure 9.** Sinusoidal tracking results: (a) Position control, (b) stiffness control.

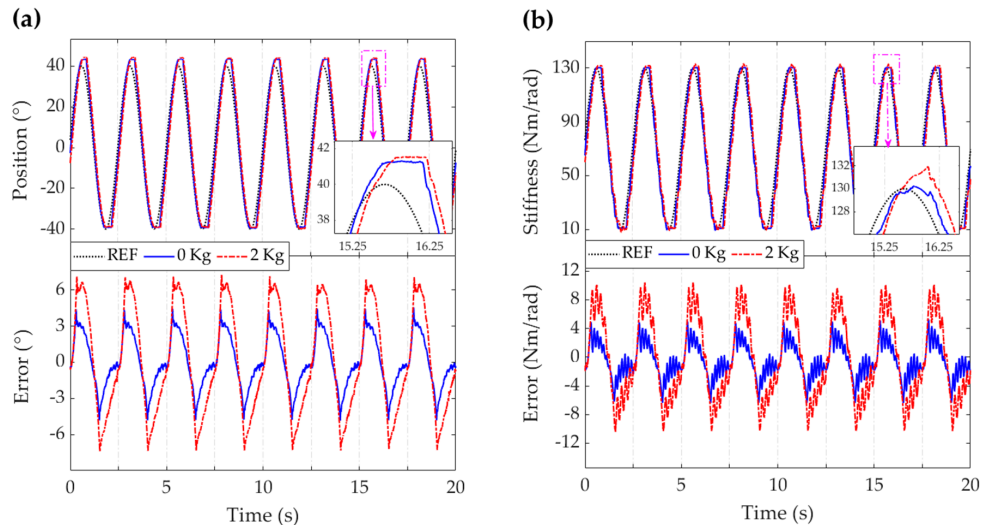


**Figure 10.** Simultaneous control for the no-load and the 2 kg load conditions. (a) Position tracking, (b) stiffness tracking.

### 5.3. Actual Stiffness Reflection

In order to assess the honesty of the ASRA in different stiffnesses, the output link is set up so that it touches the wall. The experiment is repeated with each position of the circular module (from 2.5 mm to 10 mm), it implies that the stiffness is stable, whilst only the position of the principal cylinder is changed. The deflection angle  $\theta$  is derived from the output position disparity between the principal cylinder,  $q_1$ , and the actual output link,  $q$ , which means that the related signals are measured from the optical encoder and position transducer. In the meantime, the actual interacting torque is determined by the load cell. As a result, in Figure 11, the slope of the torque arm is a reflection of the stiffness of the joint using ASRA, which is proportionately increased as the position of the circular module increases. In detail, the theoretical torque curve and the actual output torque are the dashed and the solid lines, respectively. Furthermore, the hysteresis phenomenon of the output torque can be recognized during the inflation and deflation phase, which tends to be inversely proportional to

stiffness. This hysteresis can be considered as the mechanical specificity of internal friction and the backlash of those components in each other.

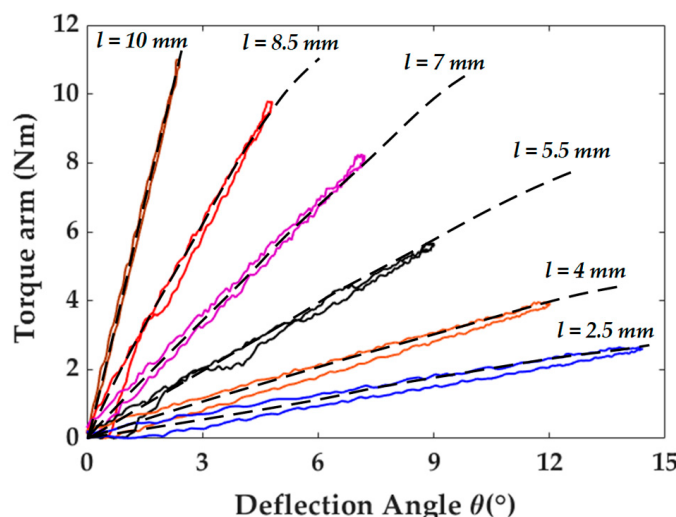


**Figure 11.** Stiffness reflection curve investigation.

## 6. Conclusions

In this work, the new compact actuator called the ARSA and its mechanical design, modeling, and control in experimental verification were presented. Due to an antagonistic configuration, this design brings out a significant efficiency of the elastic energy storage as well as minimizes the friction in the new force transmission mechanism. The designed miniaturization is achieved using a novel rotary spring module. It was noted that a three-spoke output element works as a linking basement for the output link, which links three pairs of antagonistically linear springs. The mathematical model of the actuator was analyzed in simulation and the proposed control scheme was applied to verify the fidelity of the ASRA. For evaluating the overall system, several experimental trials were accomplished by a series of scenarios with different external load conditions. The experimentally preliminary results of the ASRA showed the capability of adjustable stiffness impedances within a high accuracy with good fidelity. For future work, additional studies may include further development of the control scheme to take advantage of the ability to rapidly transform from “stiff” to “soft” and vice versa of the stiffness adjustment according to the safety and real application needs.

**Author Contributions:** K.K.A. was the supervisor providing funding and administrating the project, and he reviewed and edited the manuscript. C.P.V. carried out the investigation, methodology, analysis, and validation, and wrote the original manuscript. V.D.P. supported the implementation of simulations in MATLAB and necessary figures. T.H.N. supported the research design. All authors have read and agreed to the published version of the manuscript.

**Funding:** This work was supported by the Basic Science Research Program through the National Research Foundation of Korea (NRF), funded by the Ministry of Science and ICT, South Korea, under Grant NRF-2020R1A2B5B03001480.

**Conflicts of Interest:** The authors declare no conflict of interest.

## References

- Lee, Y.-F.; Chu, C.-Y.; Xu, J.-Y.; Lan, C.-C. A Humanoid Robotic Wrist With Two-Dimensional Series Elastic Actuation for Accurate Force/Torque Interaction. *IEEE/ASME Trans. Mechatron.* **2016**, *21*, 1315–1325. [\[CrossRef\]](#)
- Groothuis, S.S.; Rusticelli, G.; Zucchelli, A.; Stramigioli, S.; Carloni, R. The Variable Stiffness Actuator vsaUT-II: Mechanical Design, Modeling, and Identification. *IEEE/ASME Trans. Mechatron.* **2014**, *19*, 589–597. [\[CrossRef\]](#)

3. Groothuis, S.; Carloni, R.; Stramigioli, S. A Novel Variable Stiffness Mechanism Capable of an Infinite Stiffness Range and Unlimited Decoupled Output Motion. *Actuators* **2014**, *3*, 107–123. [[CrossRef](#)]
4. Malosio, M.; Spagnuolo, G.; Prini, A.; Molinari Tosatti, L.; Legnani, G. Principle of operation of RotWWC-VSA, a multi-turn rotational variable stiffness actuator. *Mech. Mach. Theory* **2017**, *116*, 34–49. [[CrossRef](#)]
5. Cestari, M.; Sanz-Merodio, D.; Garcia, E. A New and Versatile Adjustable Rigidity Actuator with Add-on Locking Mechanism (ARES-XL). *Actuators* **2018**, *7*, 1. [[CrossRef](#)]
6. Jafari, A.; Tsagarakis, N.G.; Caldwell, D.G. A Novel Intrinsically Energy Efficient Actuator With Adjustable Stiffness (AwAS). *IEEE/ASME Trans. Mechatron.* **2013**, *18*, 355–365. [[CrossRef](#)]
7. Seo, J.; Kim, J.; Park, S.; Cho, J. A SLIP-based Robot Leg for Decoupled Spring-like Behavior: Design and Evaluation. *Int. J. Control Autom. Syst.* **2019**, *17*, 2388–2399. [[CrossRef](#)]
8. DeBoon, B.; Nokleby, S.; Delfa, N.L.; Rossa, C. Differentially-Clutched Series Elastic Actuator for Robot-Aided Musculoskeletal Rehabilitation. In Proceedings of the International Conference on Robotics and Automation (ICRA), Montreal, QC, Canada, 20–24 May 2019; pp. 1507–1513.
9. Yu, H. A Novel Compact Compliant Actuator Design for Rehabilitation Robots. In Proceedings of the IEEE 13th International Conference on Rehabilitation Robotics (ICORR), Seattle, WA, USA, 24–26 June 2013; pp. 1–6.
10. Yu, H.; Huang, S.; Chen, G.; Thakor, N. Control design of a novel compliant actuator for rehabilitation robots. *Mechatronics* **2013**, *23*, 1072–1083. [[CrossRef](#)]
11. Zhu, T.; Xia, Z.; Dong, J.; Zhao, Q. A Sociable Human-robot Interaction Scheme Based on Body Emotion Analysis. *Int. J. Control Autom. Syst.* **2019**, *17*, 474–485. [[CrossRef](#)]
12. Yazdani, M.; Salarieh, H.; Foumani, M.S. Bio-inspired Decentralized Architecture for Walking of a 5-link Biped Robot with Compliant Knee Joints. *Int. J. Control Autom. Syst.* **2018**, *16*, 2935–2947. [[CrossRef](#)]
13. Kim, B.H. Analysis on Effective Rehabilitation of Human Arms Using Compliant Strap. *Int. J. Control Autom. Syst.* **2018**, *16*, 2958–2965. [[CrossRef](#)]
14. Su, H.; Sandoval, J.; Vieyres, P.; Poisson, G.; Ferrigno, G.; Momi, E.D. Safety-enhanced Collaborative Framework for Tele-operated Minimally Invasive Surgery Using a 7-DoF Torque-controlled Robot. *Int. J. Control Autom. Syst.* **2018**, *16*, 2915–2923. [[CrossRef](#)]
15. Vo, C.P.; To, X.D.; Ahn, K.K. Variable Impedance Control for a Robotic Leg with External Uncertainties. In Proceedings of the IEEE 23rd International Conference on Mechatronics Technology (ICMT), Salerno, Italy, 23–26 October 2019; pp. 1–5.
16. Lavate, S.; Todkar, R. Variable Stiffness Actuators: A General Review. *Int. J. Eng. Res.* **2015**, *4*, 201–205.
17. Marchal-Crespo, L.; Reinkensmeyer, D.J. Review of control strategies for robotic movement training after neurologic injury. *J. Neuroeng. Rehabil.* **2009**, *6*, 1–20. [[CrossRef](#)]
18. Wolf, S.; Grioli, G.; Eiberger, O.; Friedl, W.; Grebenstein, M.; Hoppner, H.; Burdet, E.; Caldwell, D.G.; Carloni, R.; Catalano, M.G.; et al. Variable Stiffness Actuators: Review on Design and Components. *IEEE/ASME Trans. Mechatron.* **2016**, *21*, 2418–2430. [[CrossRef](#)]
19. Tagliamonte, N.L.; Sergi, F.; Accoto, D.; Carpino, G.; Guglielmelli, E. Double actuation architectures for rendering variable impedance in compliant robots: A review. *Mechatronics* **2012**, *22*, 1187–1203. [[CrossRef](#)]
20. Kim, B.; Song, J. Design and Control of a Variable Stiffness Actuator Based on Adjustable Moment Arm. *IEEE Trans. Robot.* **2012**, *28*, 1145–1151.
21. Ham, R.V.; Vanderborght, B.; Damme, M.V.; Verrelst, B.; Lefever, D. MACCEPA: The mechanically adjustable compliance and controllable equilibrium position actuator for ‘controlled passive walking’. In Proceedings of the IEEE International Conference on Robotics and Automation (ICRA), Orlando, FL, USA, 15–19 May 2006; pp. 2195–2200.
22. Van Ham, R.; Vanderborght, B.; Van Damme, M.; Verrelst, B.; Lefever, D. MACCEPA, the mechanically adjustable compliance and controllable equilibrium position actuator: Design and implementation in a biped robot. *Robot. Auton. Syst.* **2007**, *55*, 761–768. [[CrossRef](#)]
23. Lee, H.; Moon, J.; Kang, T. Design of a Series Elastic Tendon Actuator Based on Gait Analysis for a Walking Assistance Exosuit. *Int. J. Control Autom. Syst.* **2019**, *17*, 2940–2947. [[CrossRef](#)]
24. Ham, R.; Sugar, T.; Vanderborght, B.; Hollander, K.; Lefever, D. Compliant actuator designs. *IEEE Robot. Autom. Mag.* **2009**, *16*, 81–94. [[CrossRef](#)]

25. Vanderborght, B.; Tsagarakis, N.G.; Semini, C.; Ham, R.V.; Caldwell, D.G. MACCEPA 2.0: Adjustable compliant actuator with stiffening characteristic for energy efficient hopping. In Proceedings of the IEEE International Conference on Robotics and Automation (ICRA), Kobe, Japan, 12–17 May 2009; pp. 544–549.
26. Hirzinger, S.W.a.G. A New Variable Stiffness Design: Matching Requirements of the Next Robot Generation. In Proceedings of the IEEE International Conference on Robotics and Automation (ICRA), Pasadena, CA, USA, 19–23 May 2008; pp. 1741–1746.
27. Wolf, S.; Feenders, J. Modeling and benchmarking energy efficiency of Variable Stiffness Actuators on the example of the DLR FSJ. In Proceedings of the 2016 IEEE/RSJ International Conference on Intelligent Robots and Systems (IROS), Daejeon, Korea, 9–14 October 2016; pp. 529–536.
28. Kim, B.; Song, J. Hybrid dual actuator unit: A design of a variable stiffness actuator based on an adjustable moment arm mechanism. In Proceedings of the IEEE International Conference on Robotics and Automation, Anchorage, AK, USA, 3–7 May 2010; pp. 1655–1660.
29. Grioli, G.; Wolf, S.; Garabini, M.; Catalano, M.; Burdet, E.; Caldwell, D.; Carloni, R.; Friedl, W.; Grebenstein, M.; Laffranchi, M.; et al. Variable stiffness actuators: The user’s point of view. *Int. J. Robot. Res.* **2015**, *34*, 727–743. [[CrossRef](#)]
30. Choi, J.; Hong, S.; Lee, W.; Kang, S.; Kim, M. A Robot Joint With Variable Stiffness Using Leaf Springs. *IEEE Trans. Robot.* **2011**, *27*, 229–238. [[CrossRef](#)]
31. Jin, H.Z.; Yang, D.C.; Zhang, H.; Liu, Z.X.; Zhao, J. Flexible Actuator With Variable Stiffness and Its Decoupling Control Algorithm: Principle Prototype Design and Experimental Verification. *IEEE/ASME Trans. Mechatron.* **2018**, *23*, 1279–1291. [[CrossRef](#)]
32. Tonietti, G.; Schiavi, R.; Bicchi, A. Design and Control of a Variable Stiffness Actuator for Safe and Fast Physical Human/Robot Interaction. In Proceedings of the IEEE International Conference on Robotics and Automation, Barcelona, Spain, 18–22 April 2005; pp. 526–531.
33. Schiavi, R.; Grioli, G.; Sen, S.; Bicchi, A. VSA-II: A Novel Prototype of Variable Stiffness Actuator for Safe and Performing Robots Interacting with Humans. In Proceedings of the IEEE International Conference on Robotics and Automation, Pasadena, CA, USA, 19–23 May 2008; pp. 2171–2176.
34. Sun, J.T.; Guo, Z.; Zhang, Y.B.; Xiao, X.H.; Tan, J.R. A Novel Design of Serial Variable Stiffness Actuator Based on an Archimedean Spiral Relocation Mechanism. *IEEE/ASME Trans. Mechatron.* **2018**, *23*, 2121–2131. [[CrossRef](#)]
35. Sun, J.T.; Guo, Z.; Sun, D.Y.; He, S.Y.; Xiao, X.H. Design, modeling and control of a novel compact, energy-efficient, and rotational serial variable stiffness actuator (SVSA-II). *Mech. Mach. Theory* **2018**, *130*, 123–136. [[CrossRef](#)]
36. Zhao, L.; Zheng, C.; Wang, Y.; Liu, B. A Finite-Time Control for a Pneumatic Cylinder Servo System Based on a Super-Twisting Extended State Observer. *IEEE Trans. Syst. Man Cybern. Syst.* **2019**, *1*–10. [[CrossRef](#)]
37. Vo, C.P.; To, X.D.; Ahn, K.K. A Novel Adaptive Gain Integral Terminal Sliding Mode Control Scheme of a Pneumatic Artificial Muscle System With Time-Delay Estimation. *IEEE Access* **2019**, *7*, 141133–141143. [[CrossRef](#)]
38. Saleh, M. Adaptive Global Terminal Sliding Mode Control Scheme with Improved Dynamic Surface for Uncertain Nonlinear Systems. *Int. J. Control Autom. Syst.* **2018**, *16*, 1692–1700.
39. Vo, C.P.; To, X.D.; Ahn, K.K. A Novel Force Sensorless Reflecting Control for Bilateral Haptic Teleoperation System. *IEEE Access* **2020**, *8*, 96515–96527. [[CrossRef](#)]

**Publisher’s Note:** MDPI stays neutral with regard to jurisdictional claims in published maps and institutional affiliations.



© 2020 by the authors. Licensee MDPI, Basel, Switzerland. This article is an open access article distributed under the terms and conditions of the Creative Commons Attribution (CC BY) license (<http://creativecommons.org/licenses/by/4.0/>).